

# The response of thick ( $10\ \mu\text{m}$ ) AlInP x-ray and $\gamma$ -ray detectors at up to 88 keV

Cite as: J. Appl. Phys. **129**, 243105 (2021); <https://doi.org/10.1063/5.0050751>

Submitted: 18 March 2021 . Accepted: 05 June 2021 . Published Online: 25 June 2021

 G. Lioliou, S. Butera,  A. B. Krysa, and A. M. Barnett



View Online



Export Citation



CrossMark

## ARTICLES YOU MAY BE INTERESTED IN

[Multi-junction solar cells paving the way for super high-efficiency](#)

Journal of Applied Physics **129**, 240901 (2021); <https://doi.org/10.1063/5.0048653>

[Recent developments of quantum sensing under pressurized environment using the nitrogen vacancy \(NV\) center in diamond](#)

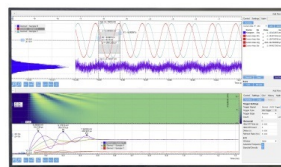
Journal of Applied Physics **129**, 241101 (2021); <https://doi.org/10.1063/5.0052233>

[Terahertz emission spectroscopy of GaN-based heterostructures](#)

Journal of Applied Physics **129**, 245702 (2021); <https://doi.org/10.1063/5.0047402>

Challenge us.

What are your needs for  
periodic signal detection?



Zurich  
Instruments



# The response of thick ( $10\ \mu\text{m}$ ) AlInP x-ray and $\gamma$ -ray detectors at up to 88 keV

Cite as: J. Appl. Phys. **129**, 243105 (2021); doi: [10.1063/5.0050751](https://doi.org/10.1063/5.0050751)

Submitted: 18 March 2021 · Accepted: 5 June 2021 ·

Published Online: 25 June 2021



G. Lioliou,<sup>1,a)</sup>  S. Butera,<sup>1</sup> A. B. Krysa,<sup>2</sup>  and A. M. Barnett<sup>1</sup>

## AFFILIATIONS

<sup>1</sup>Space Research Group, School of Mathematical and Physical Sciences, University of Sussex, Brighton BN1 9QT, United Kingdom

<sup>2</sup>EPSRC National Epitaxy Facility, Department of Electrical and Electronic Engineering, University of Sheffield, Mappin Street, Sheffield S1 3JD, United Kingdom

<sup>a)</sup>Author to whom correspondence should be addressed: [G.Lioliou@sussex.ac.uk](mailto:G.Lioliou@sussex.ac.uk). Tel.: +44 (0) 1273 872568

## ABSTRACT

The development of new x-ray and  $\gamma$ -ray spectrometers based on AlInP photodiodes with increased quantum detection efficiency and improved energy resolution is reported. The spectroscopic responses of two AlInP  $p^+i-n^+$  mesa photodiodes ( $10\ \mu\text{m}$  i layer, the thickest so far reported) were investigated at photon energies from 4.95 to 88.03 keV; the detectors and preamplifier were operated at 30 °C. Energy resolutions (full width at half maximum) of  $750 \pm 40\ \text{eV}$  and  $850 \pm 30\ \text{eV}$  at 4.95 keV were achieved with the two detectors. The energy resolution deteriorated with increasing photon energy; this was in accordance with the increasing Fano noise with energy and suggested negligible incomplete charge collection noise across the photon energy range investigated. The measured voltage output of each spectrometer was found to be linear as a function of incident x-ray photon energy. The count rate (measured at 8.63 keV) was also found to linearly increase with incoming x-ray photon flux for the investigated spectrometers. These results, which were obtained using the thickest AlInP photodiodes produced so far, suggest that AlInP detectors are highly promising candidates for future uncooled x-ray and  $\gamma$ -ray spectrometers.

Published under an exclusive license by AIP Publishing. <https://doi.org/10.1063/5.0050751>

## I. INTRODUCTION

Although the energy resolutions achieved with high quality cooled Si and Ge x-ray and  $\gamma$ -ray detectors coupled to ultra-low-noise front end electronics are close to their theoretical limits,<sup>1–3</sup> other semiconductor materials, such as SiC,<sup>4,5</sup> GaAs,<sup>6–10</sup> AlGaAs,<sup>11–13</sup> In<sub>0.5</sub>Ga<sub>0.5</sub>P,<sup>14,15</sup> and CdZnTe,<sup>16,17</sup> are under active development for use in the applications, which require high temperature tolerant, radiation hard, and/or high detection efficiency detectors. A variety of semiconductor radiation detectors have been, and are being, developed to meet the requirements of various applications that predominantly require the deployment of such instrumentation in harsh environments (e.g., spaceflight, nuclear science and engineering, and defense systems).

Recently, Al<sub>0.52</sub>In<sub>0.48</sub>P detectors have drawn attention as potentially suitable candidates for photon counting x-ray and  $\gamma$ -ray spectroscopy. The relatively large linear absorption coefficient of Al<sub>0.52</sub>In<sub>0.48</sub>P at hard photons energies (e.g.,  $12.23\ \text{cm}^{-1}$  at 60 keV), cf. Si ( $0.30\ \text{cm}^{-1}$  at 60 keV), Ge ( $9.45\ \text{cm}^{-1}$  at 60 keV), SiC ( $0.30\ \text{cm}^{-1}$  at 60 keV), GaAs ( $9.54\ \text{cm}^{-1}$  at 60 keV), and AlGaAs ( $6.30\ \text{cm}^{-1}$  at 60 keV, for Al<sub>0.8</sub>Ga<sub>0.2</sub>As),<sup>18</sup> results in increased

quantum detection efficiencies per unit thickness; the relatively wide bandgap of Al<sub>0.52</sub>In<sub>0.48</sub>P (2.31 eV,<sup>19</sup> cf. 1.12 eV for Si<sup>20</sup> and 0.66 eV for Ge,<sup>21</sup> all at 300 K) enables uncooled operation at high temperatures (>20 °C). Moreover, Al<sub>0.52</sub>In<sub>0.48</sub>P is the widest bandgap semiconductor that can be grown lattice matched upon GaAs substrates,<sup>22</sup> potentially enabling defect-free epilayer growth and facilitating commercial production.

Al<sub>0.52</sub>In<sub>0.48</sub>P  $p^+i-n^+$  photodiodes with progressively increasing i layer thickness, and thus increasing quantum detection efficiency, have been investigated for photon counting x-ray spectroscopy;  $2\ \mu\text{m}$ <sup>23,24</sup> and  $6\ \mu\text{m}$ <sup>25,26</sup> thick i layers have recently been shown to operate as photon counting x-ray detectors (at 5.9 keV) at temperatures up to 100 °C.<sup>24,26</sup> In contrast to the early Al<sub>0.52</sub>In<sub>0.48</sub>P x-ray photodiodes that suffered from incomplete charge collection noise, more recent devices have been reported without such phenomena.<sup>27,28</sup>

Here, new results are reported that characterize the thickest ( $10\ \mu\text{m}$  i layer) Al<sub>0.52</sub>In<sub>0.48</sub>P detectors so far reported. Two detectors of different diameters (D1,  $200\ \mu\text{m}$ ; D2,  $400\ \mu\text{m}$ ) were investigated. The detectors were illuminated with x-rays and  $\gamma$ -rays of characteristic energies from 4.95 to 88.03 keV, thus providing the

widest energy range so far used to characterize detectors made of this material. At first, the detectors were illuminated with x-ray fluorescence photons from high-purity metal calibration foils (giving characteristic energies from 4.95 to 21.17 keV); the foils were fluoresced using x-rays from a Mo target x-ray tube. Second, the detectors were illuminated directly with photons from  $^{241}\text{Am}$  and  $^{109}\text{Cd}$  radioisotope x-ray and  $\gamma$ -ray sources, emitting photons of energy up to 59.54 and 88.03 keV, respectively. The voltage output and energy resolution of the spectrometers as functions of incoming photon energy, and the count rate as a function of incident photon flux, were investigated.

## II. DETECTOR STRUCTURE

An  $\text{Al}_{0.52}\text{In}_{0.48}\text{P}$  (herein after AlInP)  $\text{p}^+-\text{i}-\text{n}^+$  epi-structure was grown by metalorganic vapor phase epitaxy (MOVPE) on a commercial (100)  $\text{n}^+$  GaAs:Si substrate. It consisted of a  $0.2\ \mu\text{m}$  GaAs buffer layer; 0.1, 10, and  $0.2\ \mu\text{m}$  AlInP  $\text{n}^+$ , i, and  $\text{p}^+$  layers; and a  $0.01\ \mu\text{m}$  GaAs cap layer that was deposited atop the structure to help achieve a good Ohmic top contact. The AlInP layer structure is summarized in Table I and a schematic diagram is shown in Fig. 1. The wafer was processed to produce circular mesa photodiodes (bevel angle of  $>30^\circ$ ) using standard photolithography and wet chemical etching techniques; a  $200\ \mu\text{m}$  diameter device (D1) and a  $400\ \mu\text{m}$  diameter device (D2) were fabricated. The primary chemical etchant was  $\text{K}_2\text{Cr}_2\text{O}_7\text{:HBr:CH}_3\text{COOH}$  (1:1:1), augmented by a 10 s  $\text{H}_2\text{SO}_4\text{:H}_2\text{O}_2\text{:H}_2\text{O}$  (1:8:80) finishing etch. Ohmic Ti/Au (20 nm/200 nm) metal contacts were evaporated onto the top of the devices; the metallization was of a quasi-annular design with an enlarged area bond pad, and it covered 45% and 33% of the faces of D1 and D2, respectively. The geometry of the metallization was similar to that show in Fig. 1 of Ref. 29. The two devices were on a single die and a planar Ohmic InGe/Au (20 nm/200 nm) metal contact was deposited onto the rear of the GaAs substrate. The photodiodes were packaged in a TO-5 can and gold ball-wedge bonded wire.

The quantum detection efficiency of the detectors, shown in Fig. 2, was calculated as a function of incident photon energy, taking into account the photon attenuation within the dead layers (Au/Ti top contact, the GaAs contact layer, and the  $\text{p}^+$  layer) and the photon absorption within the active layer (depleted i layer). The linear attenuation and absorption coefficients of the component elements were assumed to be as per Ref. 18. The calculated quantum detection efficiency of and assuming that only the i layer

TABLE I. Layer details of the AlInP  $\text{p}^+-\text{i}-\text{n}^+$  structure.

Material	Type	Dopant	Thickness ( $\mu\text{m}$ )	Doping density ( $\text{cm}^{-3}$ )
GaAs	$\text{p}^+$	Zn	0.01	$1 \times 10^{19}$
AlInP	$\text{p}^+$	Zn	0.2	$5 \times 10^{17}$
AlInP	i	–	10	Undoped
AlInP	$\text{n}^+$	Si	0.1	$2 \times 10^{18}$
GaAs	$\text{n}^+$ (buffer)	Si	0.2	$2 \times 10^{18}$
GaAs	$\text{n}^+$ (substrate)	Si	350	$2 \times 10^{18}$

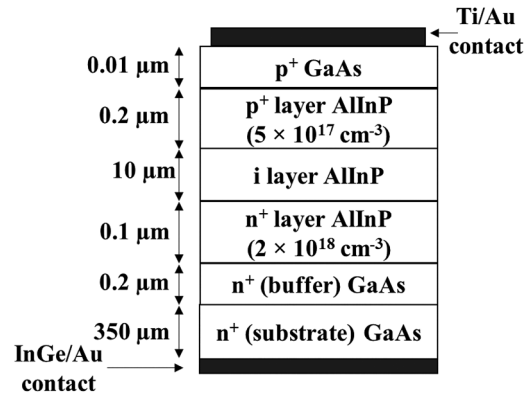


FIG. 1. Schematic diagram of the layer details of the AlInP  $\text{p}^+-\text{i}-\text{n}^+$  structure.

contributed to detection (i.e., charge created in the  $\text{p}^+$  and  $\text{n}^+$  layers was lost), the quantum detection efficiency was 0.75 for D1 and 0.77 for D2 at 4.95 keV and 0.0041 for both detectors at 88 keV. However, as will be shown in Sec. III, the detectors were operated at a reverse bias of 150 V, which resulted in an  $8.1\ \mu\text{m}$  depletion layer thickness (see Sec. III); with the detectors operated in this condition and using the same assumptions again for the active and inactive regions, the quantum detection efficiency was 0.70 for D1 and 0.72 for D2 at 4.95 keV and 0.0033 for both detectors at 88 keV. The difference in the quantum detection efficiency between the two detectors at relatively low photon energies was attributed to the difference in the fraction of the area covered by the top Ohmic contacts between the two detectors. It should be noted here that the quantum detection efficiency corresponds to the useful interaction of the incident to the detector face photons with the active layer of the detector. The resulting quanta of such an interaction (photoelectric absorption being the dominant mechanism within the investigated energy range), namely, the ejected photoelectron and the emitted characteristic x-ray fluorescence of the semiconductor detector, may not be

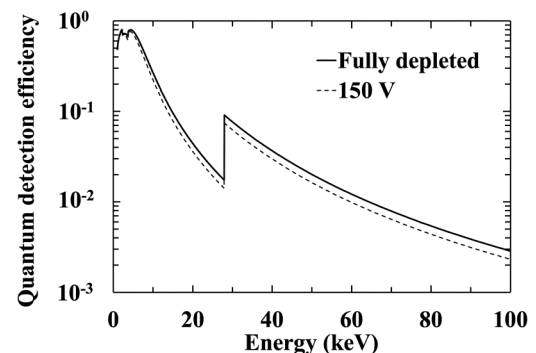


FIG. 2. Quantum detection efficiency of D1 as a function of photon energy when (a) fully depleted (solid line) and (b) operated at 150 V reverse bias (dashed line).

fully absorbed within the active layer of the detector, resulting in fluorescence peaks and escape peaks, as shown in Sec. VI.

### III. DETECTOR ELECTRICAL CHARACTERIZATION

The electrical characteristics (leakage current and capacitance as functions of applied reverse bias) of each detector were measured at 30 °C; determination of such characteristics is important since they affect the detectors' spectroscopic performances.<sup>50</sup> A Temperature Applied Sciences Limited<sup>31</sup> Micro MT climatic cabinet was used for temperature control, and the detectors were installed within a light-tight, electromagnetically screened test harness within the chamber. The environment of the detectors was purged with dry N<sub>2</sub> (relative humidity of <5%) in order to exclude any humidity related effects.<sup>32</sup> A Keithley 6487 Picoammeter/Voltage Source and an HP 4275A Multi Frequency LCR meter (with a sinusoidal test signal of 50 mV rms magnitude and 1 MHz frequency) were used for the leakage current and capacitance measurements, respectively. The devices were investigated across an applied reverse bias range of 0–200 V, in 5 V steps. A temperature of 30 °C was used since this was the temperature at which the detectors were operated during later spectroscopic measurements.

The measured leakage currents of the packaged AllnP detectors are shown in Fig. 3. The leakage current of the package was subsequently measured separately and subtracted from the measured total leakage current, since the measured total leakage current included the contribution from the TO-5 can in addition to the photodiode itself. The resultant leakage currents of the AllnP photodiodes themselves are also shown in Fig. 3. At the maximum applied reverse bias (200 V), the total leakage current was  $3.3 \pm 0.4$  pA for D1 with its package ( $1.9 \pm 0.6$  pA, D1 itself) and  $3.7 \pm 0.4$  pA for D2 with its package ( $2.4 \pm 0.6$  pA, D2 itself).

The leakage current of photodiodes can have two origins, the bulk (volume) and the surface; the part that arises from the bulk of the photodiode is directly proportional to the device's area, whereas the part that arises from the surface of the photodiode is directly proportional to the device's circumference. Given the radii

of D1 ( $=100 \mu\text{m}$ ) and D2 ( $=200 \mu\text{m}$ ), the ratio of the area of D1 to that of D2 was 0.25, whereas the ratio of the circumference of D1 to that of D2 was 0.5. The ratio of the measured leakage current at 200 V of D1 to that of D2 was  $0.8 \pm 0.3$ . This suggested that the main origin of the leakage current was not from the bulk; however, considering the uncertainty of this ratio, it was inconclusive as to whether the devices had the same leakage current at 200 V or D1 had a leakage current at 200 V 0.5 of that of D2 (i.e., the leakage current originated from the surface). The leakage current density was then calculated in each case, to verify the above findings, by dividing the leakage current of the photodiode itself by its respective area, assuming the leakage current originated in the bulk and that the quality of the wafer was uniform; it was found to be  $6 \pm 2 \text{ nA cm}^{-2}$  and  $1.9 \pm 0.5 \text{ nA cm}^{-2}$  at 200 V applied reverse bias for D1 and D2, respectively. Since the values do not match (i.e., the leakage currents did not scale with the area of the photodiodes), it appears that surface leakage currents arising from the mesa edges contributed significantly to the total, while the contribution of the bulk leakage current was not excluded entirely. Leakage current measurements for multiple devices of each size would have given a better insight into the origin of the leakage current. The white parallel (WP) noise contribution was calculated as per Ref. 30 and can be seen in Fig. 3; it was found to be  $6 \pm 5 \text{ e}^- \text{ rms}$  ( $9 \pm 5 \text{ e}^- \text{ rms}$ , including the package) and  $9 \pm 5 \text{ e}^- \text{ rms}$  ( $11 \pm 5 \text{ e}^- \text{ rms}$ , including the package) for D1 and D2, respectively, at 150 V applied reverse bias and  $2 \mu\text{s}$  shaping time. For comparison, this is broadly similar to other high quality wide bandgap x-ray detectors operated at the same temperature, e.g.,  $13 \text{ e}^- \text{ rms}$  for a  $10 \mu\text{m}$  thick GaAs photodiode<sup>9</sup> and  $\leq 8 \text{ e}^- \text{ rms}$  for a  $5 \mu\text{m}$  i layer thick InGaP photodiode<sup>14</sup> under their normal operating conditions and at a temperature  $\approx 30$  °C.

The capacitance of each packaged photodiode was measured; the depletion layer capacitance of the photodiodes themselves, shown in Fig. 4, was calculated by subtracting the empty package capacitance (measured separately) from the total capacitance. The depletion layer capacitance of D1 decreased from  $2.61 \pm 0.03$  pF at 0 V to  $0.36 \pm 0.03$  pF at 200 V and that of D2 decreased from  $10.09 \pm 0.03$  pF at 0 V to  $1.42 \pm 0.03$  pF at 200 V. The ratio of the

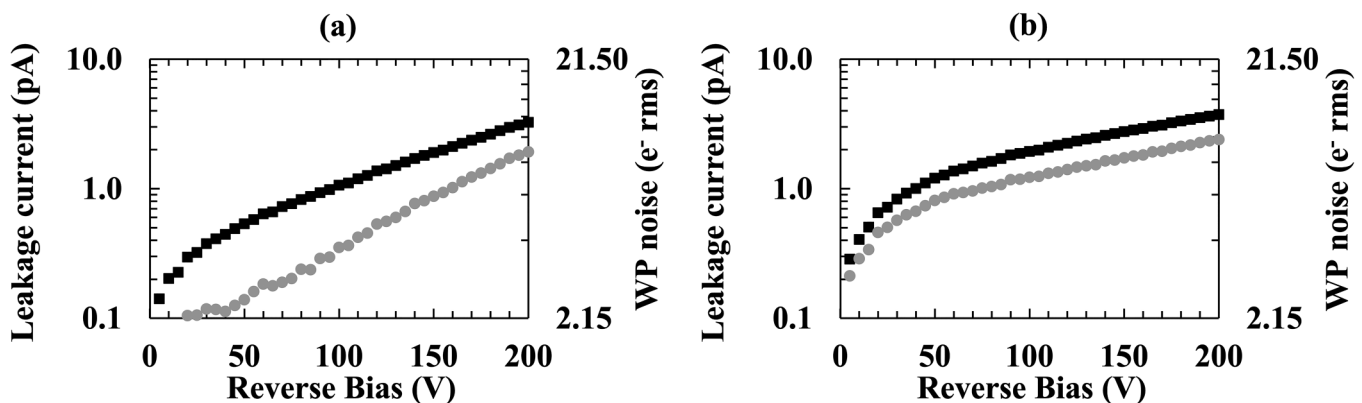
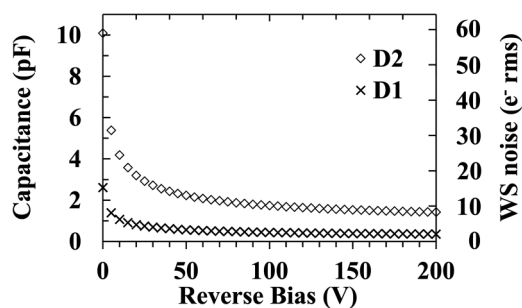


FIG. 3. Leakage current and associated white parallel (WP) noise at  $2 \mu\text{s}$  shaping time, as a function of applied reverse bias for (a) D1 and (b) D2, when packaged (black squares) and from the photodiodes themselves (gray circles), at 30 °C. The error bars were omitted for clarity.



**FIG. 4.** Depletion layer capacitance and associated white series (WS) noise at  $2 \mu\text{s}$  shaping time, as a function of applied reverse bias for D1 ( $\times$  symbols) and D2 (open diamonds), at  $30^\circ\text{C}$ . The error bars are smaller than the symbol sizes and have thus been omitted.

D1 and D2 capacitances ( $=4$ ) was consistent with the ratio of their areas. The white series (WS) noise contribution was calculated (as per Ref. 32) and can also be seen in Fig. 4; it was found to be  $2.3 \pm 0.2 e^- \text{ rms}$  and  $9.0 \pm 0.2 e^- \text{ rms}$  for D1 and D2, respectively, at  $150 \text{ V}$  applied reverse bias and  $2 \mu\text{s}$  shaping time.

The depletion layer width of each photodiode was calculated as a function of applied reverse bias from the depletion layer capacitance (assuming a parallel plate capacitance<sup>21</sup>) and can be seen in Fig. 5. The depletion depth increased from  $1.198 \pm 0.004 \mu\text{m}$  at  $0 \text{ V}$  to  $8.8 \pm 0.2 \mu\text{m}$  at  $200 \text{ V}$  for D1 and from  $1.241 \pm 0.002 \mu\text{m}$  at  $0 \text{ V}$  to  $8.80 \pm 0.05 \mu\text{m}$  at  $200 \text{ V}$  for D2. The maximum depletion depth measured was  $9 \pm 2 \mu\text{m}$  for D1 and  $8.8 \pm 0.6 \mu\text{m}$  for D2, taking into account the repeatability accuracy and the Debye length ( $0.1 \mu\text{m}$ ) in addition to the LCR uncertainty. Both detectors had a depletion layer width of  $8.1 \mu\text{m}$  when operated at  $150 \text{ V}$  applied reverse bias. Although not fully depleted under the operating conditions used

here, the detectors still had higher quantum detection efficiency (Fig. 2) compared to previously reported AlInP detectors, which had depletion widths of  $1.97 \pm 0.05 \mu\text{m}$ <sup>27</sup> and  $5.7 \pm 0.9 \mu\text{m}$ <sup>28</sup> at their operating conditions.

The effective carrier concentration within the *i* layer, as shown in Fig. 5, was extracted using the differential capacitance profiling method;<sup>21</sup> it equals the doping profile so long as the doping profile does not vary over distances less than one Debye length. Capacitance values corresponding to greater applied reverse bias steps than that measured ( $5 \text{ V}$ ) were used for the effective carrier concentration calculations to reduce the associated uncertainties. Minimum values of  $17.0 \times 10^{14} \pm 0.3 \times 10^{14} \text{ cm}^{-3}$  for D1 and  $16.1 \times 10^{14} \pm 0.1 \times 10^{14} \text{ cm}^{-3}$  for D2 were calculated (at  $1.2 \pm 0.1 \mu\text{m}$  below the  $p^+ - i$  junction). The effective carrier concentration increased upon reaching the  $i - n^+$  interface, as can be seen in Fig. 5. It reached a value of  $50 \times 10^{14} \pm 20 \times 10^{14} \text{ cm}^{-3}$  for D1 and  $58 \times 10^{14} \pm 6 \times 10^{14} \text{ cm}^{-3}$  for D2.

#### IV. ENERGY CALIBRATION OF THE SPECTROSCOPIC SYSTEMS

Each detector was connected, in turn, to a low-noise charge-sensitive preamplifier. The preamplifier was custom-made, similar to the one in Ref. 33, and employed a Vishay Siliconix 2N4416A JFET as its input transistor. Initially, the spectroscopic response of the detectors was studied under the illumination of x-ray fluorescence photons from nine high-purity calibration foils (see Table II), which were fluoresced using a Mo target x-ray tube housed in an LD Didactic GmbH 554 801 x-ray apparatus. X-rays from the x-ray tube were collimated using an Al collimator ( $20 \text{ mm}$  in diameter) lined with polytetrafluoroethylene. The calibration foils were positioned at an angle of  $45^\circ$  with respect to the collimator. The detectors, which were in a light-tight, electromagnetically screened, Al test fixture with a  $4 \mu\text{m}$  thick Al x-ray window, were positioned

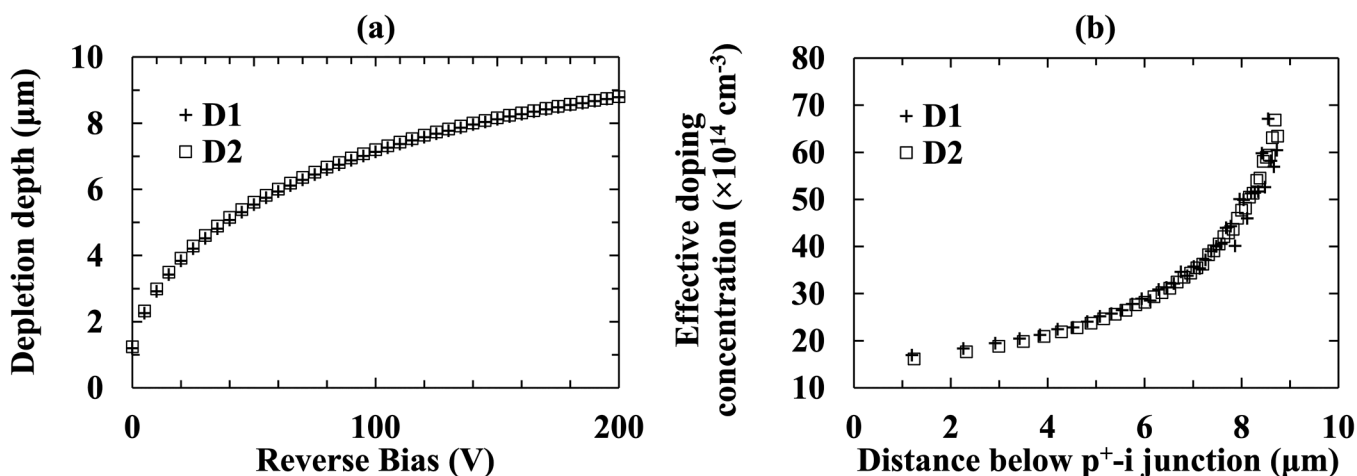


**FIG. 5.** (a) Depletion depth as a function of applied reverse bias and (b) effective carrier concentration as a function of distance below the  $p^+ - i$  junction, for D1 ( $+$  symbols) and D2 (open squares), at  $30^\circ\text{C}$ . The error bars were omitted for clarity.

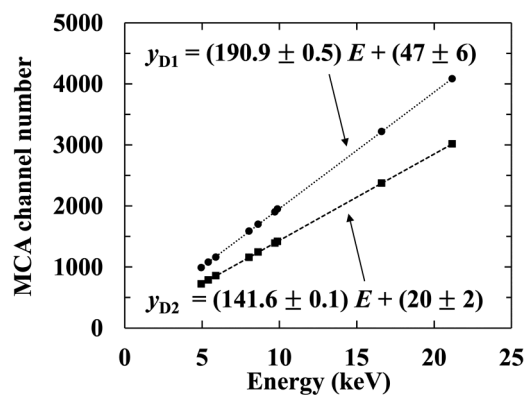
**TABLE II.** The high-purity x-ray calibration foils and their primary x-ray emission line energies.<sup>34</sup>

Material (primary line)	Line energy (keV)
V ( $K\alpha$ )	4.95
Cr ( $K\alpha$ )	5.41
Mn ( $K\alpha$ )	5.90
Cu ( $K\alpha$ )	8.04
Zn ( $K\alpha$ )	8.63
Au ( $L\alpha$ )	9.71
Ge ( $K\alpha$ )	9.88
Nb ( $K\alpha$ )	16.61
Pd ( $K\alpha$ )	21.17

at  $135^\circ$  with respect to the collimator. This arrangement minimized the detection of x rays from the x-ray tube itself and maximized the detection of fluorescence x-rays from the calibration foils. The test fixture was continually purged with dry  $N_2$  (relative humidity <5%) throughout the measurements. The x-ray tube's potential difference was set to 35 kV, and it was operated at a tube current of 1 mA. To ensure thermal equilibrium in the system was achieved, the tube was switched on and left on for 3 h prior to taking measurements. The system temperature stabilized at  $30 \pm 5^\circ\text{C}$ . The preamplifier output was shaped by an Ortec 572A shaping amplifier and digitized by a multi-channel analyzer (MCA) (Ortec Easy-MCA-8K); both the shaping amplifier and MCA were operated at room temperature.

The x-ray spectra were accumulated with each foil fluoresced in turn. Live time limits of 9600 and 2400 s were set for D1 and D2, respectively, to reflect the difference in their areas. All spectra were accumulated at a shaping time of  $2\ \mu\text{s}$  (preliminary measurements had shown that this was the best of the available shaping times, 0.5, 1, 2, 3, 6, and  $10\ \mu\text{s}$ , for the system). The detectors were reversed biased at 150 V; no improvement in energy resolution was observed at greater applied reverse biases.

Gaussians were fitted to the primary fluorescence peak in each of the accumulated x-ray spectra. In cases where more than one fluorescence peak contributed to a detected photopeak, i.e., where adjacent peaks could not be resolved individually (e.g., V  $K\alpha$  and  $K\beta$ ), they were deconvolved by computing two Gaussians, the summation of which was fitted to the measured photopeak. The relative emission ratios<sup>35</sup> and the relative quantum detection efficiencies of the detectors at these energies were taken into consideration in each case. An energy calibration for each spectrometer (i.e., that employing D1 and that employing D2) was deduced from the lines of best fit (calculated using linear least squares fitting) between the position (MCA channel number) of the centroid of each fitted fluorescence peak and its accepted photon energy,<sup>34</sup> as shown in Fig. 6. Linear relationships between the voltage output of each spectroscopic system and the incoming x-ray photon energy were found; the standard deviation of the calibrated MCA channel numbers suggested linearity within  $\pm 40$  eV (corresponding to  $\pm 8$  channels of 5 eV width each) for D1 and  $\pm 14$  eV (corresponding to  $\pm 2$  channels of 7 eV width each) for the D2, over the energy from 4.95 to 21.17 keV. The relationships

**FIG. 6.** X-ray energy response linearity of the D1 (black circles) and D2 (black squares) spectrometers. The lines of best fit, calculated using linear least squares fitting, are also shown (D1, dotted line; D2, dashed line).

describing the energy calibration of the MCA's charge scale of each spectrometer differed. This was attributed to the different capacitances of the detectors of each spectrometer (D1 and D2, see Fig. 4) and the likely presence of different stray capacitances at the input of the preamplifier due to slight differences in the connection between each detector and the input of the preamplifier. Both of these have a direct effect on the conversion factor of the preamplifier and thus on the voltage output of the spectroscopic system.

As examples of the spectra obtained with each detector, Fig. 7 shows the x-ray fluorescence spectra of the V ( $K\alpha = 4.95$  keV;  $K\beta = 5.42$  keV) calibration foil obtained using D1 and D2, respectively; spectra of this nature were accumulated for all the calibration foils. The energy calibration of the MCA's charge scale of both spectrometers was achieved using the relationships extracted in Fig. 6. The detected photopeak was the combination of the V  $K\alpha$  and  $K\beta$  emissions; Gaussian fitting was used to deconvolve the peaks, taking into account the relative emission ratio for the photons<sup>35</sup> and the relative efficiency of the detectors at 4.95 and 5.42 keV.

The energy resolutions of the spectrometers as functions of photon energy were recorded, and the results are presented in Fig. 8. The energy resolution was quantified as the full width at half maximum, FWHM, of each fitted fluorescence peak in the accumulated spectra. Due to difficulties in deconvolving the Au  $L\alpha$  and Au  $L\beta$  peaks caused by the presence of detector self-fluorescence peaks at similar energies (Ga  $K\alpha$  and  $K\beta$  and As  $K\alpha$  and  $K\beta$ ), they were excluded from Fig. 8. The FWHM increased from  $750 \pm 40$  eV at 4.95 keV to  $840 \pm 40$  eV at 21.17 keV for the spectrometer employing D1, and from  $850 \pm 30$  eV at 4.95 keV to  $890 \pm 30$  eV at 21.17 keV for the spectrometer employing D2. The uncertainties associated with the FWHM ( $\pm 40$  eV for D1 and  $\pm 30$  eV D2) resulted from the combination (error propagation) of the estimated uncertainties of determining (1) the centroid channel number of the fitted Gaussian, (2) the centroid channel number of the zero energy noise peak, and (3) the standard deviation of the fitted Gaussian.

The spectral resolution of an x-ray and  $\gamma$ -ray spectrometer using a non-avalanche photodiode as its detector is defined by the quadratic sum of the Fano noise, the electronic noise, and

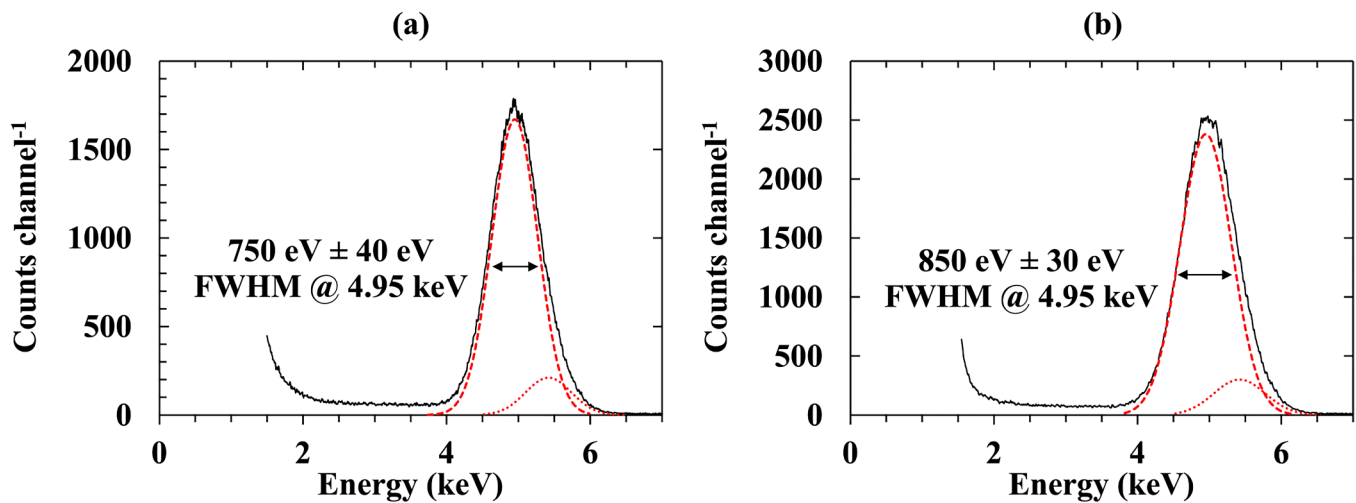


FIG. 7. V ( $K\alpha = 4.95$  keV;  $K\beta = 5.42$  keV) x-ray fluorescence spectra accumulated with (a) D1 and (b) D2. The deconvoluted V  $K\alpha$  (red dashed line) and V  $K\beta$  (red dotted line) peaks are also shown.

(if present) the incomplete charge collection noise, such that,

$$\text{FWHM (eV)} = 2.355 \sqrt{FE\omega + \left(\frac{R}{2.355}\right)^2 + AE^B}, \quad (1)$$

where  $\omega$  is the semiconductor electron-hole pair creation energy,  $F$  is the Fano factor,  $E$  is the incident photon energy,  $R$  is the electronic noise, and the third term under the square root is the incomplete charge collection noise.<sup>32,36</sup> The parameters of the incomplete

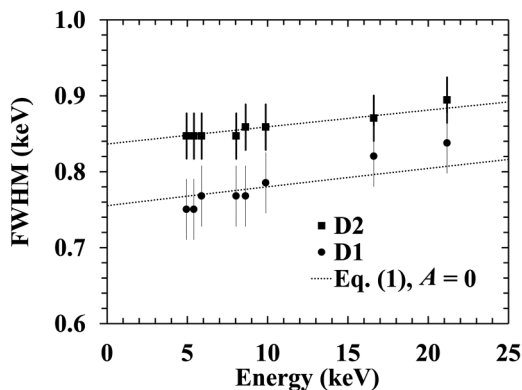


FIG. 8. Measured FWHM as a function of x-ray energy for D1 (filled circles) and D2 (filled squares). The predicted FWHM (dotted lines) as computed using Eq. (1) and  $A = 0$  is also shown; the electronic noise was extracted from the fitting (755 eV for D1; 837 eV for D2). The gradient of the predicted FWHM as a function of x-ray energy was dictated in each case by the relationship of the Fano noise to the x-ray photon energy.

charge collection noise,  $A$  and  $B$ , are semiempirical constants determined by best-fitting.<sup>7</sup> The Fano noise (i.e., when  $R = 0$  and  $A = 0$ ) is the ultimately achievable energy resolution limited by statistical fluctuations in the number of electron-hole pairs generated by the absorption of a photon. The electronic noise comprises four different noise components: parallel white noise, series white noise (including the induced gate current noise),  $1/f$  noise, and dielectric noise.<sup>32,36</sup> While the Fano noise and incomplete charge collection noise are dependent upon the incident photon energy,  $E$ , the electronic noise is photon energy invariant.

The Fano noise was estimated to be 138 eV (11  $e^-$  rms) at 4.95 keV and 285 eV (23  $e^-$  rms) at 21.17 keV, given an electron-hole pair creation energy of 5.31 eV at 30 °C<sup>37</sup> and, since the Fano factor of AlInP has not yet been reported, assuming a Fano factor of 0.13 (i.e., equal to that measured for  $\text{In}_{0.5}\text{Ga}_{0.5}\text{P}$ ,<sup>14</sup> a similar wide bandgap ternary compound semiconductor). The difference between the measured FWHM at each energy and the expected Fano noise was attributed to the electronic noise and, if present, any incomplete charge collection noise.

The presence of detectable incomplete charge collection noise was examined. Initially, the detectors were considered to have insignificant incomplete charge collection noise, i.e.,  $A = 0$ : Eq. (1) was fitted to the measured FWHM as a function of x-ray photon energy, for both spectrometers (i.e., that with D1 and that with D2). The predicted FWHM, which resulted from fitting Eq. (1) to the measured FWHM as a function of x-ray photon energy and assuming  $A = 0$ , by minimizing the sum of the squared residuals, can be seen in Fig. 8. The working hypothesis of insignificant incomplete charge collection noise, i.e., the suitability of the assumption of  $A = 0$ , was checked; the error bars associated with the fitting for each data point were computed and compared with the uncertainties of determining the FWHM at each energy. The error bars,  $S$ , were obtained from the square root of the sum of

squared residuals,  $C$ , over the number of degrees of freedom associated with the sum of squared residuals,<sup>38</sup>

$$S = \sqrt{\frac{\sum (C)^2}{n-2}}. \quad (2)$$

In Eq. (2),  $n$  is the number of data points for the fitting. The error bars were  $\pm 20$  and  $\pm 6$  eV for D1 and for D2, respectively, and smaller than the uncertainty of the FWHM in both cases ( $\pm 40$  and  $\pm 30$  eV for D1 and for D2, respectively). The extracted electronic noise was 755 eV ( $60 e^-$  rms) for D1 and 837 eV ( $67 e^-$  rms) for D2. The successful prediction of the FWHM at the investigated photon energy range (4.95–21.17 keV) with  $A = 0$  suggested the absence of significant incomplete charge collection in the reported AlInP detectors when they were operated at a reverse bias of 150 V.

To establish further the limits of any possible incomplete charge collection noise, the minimum amount of detectable incomplete charge collection noise was calculated, taking into account the predicted FWHM as a function of energy [using Eq. (1)] and the uncertainties of the measured FWHM; the 21.17 keV photon energy was considered, at which the incomplete charge collection noise was expected to have its greatest contribution. The minimum detectable incomplete charge collection noise had a lower limit of 31 and 25  $e^-$  rms for D1 and D2, respectively, suggesting that the detectors exhibited  $< 31 e^-$  rms (D1) and  $< 25 e^-$  rms (D2) incomplete charge collection noise. This is similar to as was previously reported for 6  $\mu\text{m}$   $i$  layer thick AlInP photodiodes,<sup>28</sup> which exhibited  $< 26 e^-$  rms (a 217  $\mu\text{m}$  diameter device) and  $< 40 e^-$  rms (a 409  $\mu\text{m}$  diameter device) incomplete charge collection noise, unlike thinner (2  $\mu\text{m}$   $i$  layer) AlInP devices, which contributed 36  $e^-$  rms (a 200  $\mu\text{m}$  diameter device)<sup>28</sup> and  $> 60 e^-$  rms (a 400  $\mu\text{m}$  diameter device)<sup>28</sup> of incomplete charge collection noise to the energy resolution of the corresponding spectrometers, at 21.17 keV.

The fitting of Eq. (1) to the measured FWHM as a function of x-ray photon energy was relatively insensitive to the value of the Fano factor used; Fano factor,  $F$ , values of  $0.11 \leq F \leq 0.15$  were considered and all resulted in an extracted electronic noise of  $756 \pm 4$  eV ( $60.4 \pm 0.3 e^-$  rms) for D1 and  $836 \pm 2$  eV ( $66.9 \pm 0.2 e^-$  rms) for D2. In each case, the error bars associated with the fitting were smaller than the uncertainty of the FWHM ( $\pm 40$  and  $\pm 30$  eV for D1 and for D2, respectively). As such, it is impossible to estimate the Fano factor using the currently reported multi-energy measurements. Similar future measurements using a spectroscopic system with reduced electronic noise and improved accuracy of determining the FWHM would allow the extraction of the Fano factor for AlInP.

The energy resolutions achieved may be compared with those obtained using x-ray spectrometers using different detectors but similar readout electronics and, in each case, operating at the same temperature. The detectors showed better energy resolutions compared to those achieved with earlier and thinner AlInP detectors; comparing 200  $\mu\text{m}$  diameter devices, FWHM at 21.17 keV of 1.12 keV and 880 eV have been reported for detectors with 2  $\mu\text{m}$ <sup>27</sup> and 6  $\mu\text{m}$ <sup>28</sup> thick  $i$  layers, respectively. The improvement in the present devices (10  $\mu\text{m}$  thick  $i$  layer) was, in part, attributed to a reduction in white series noise as the thickness of the  $i$  layer of the

photodiode was increased thus reducing detector capacitance; as outlined above, improved material quality also resulted in the elimination of previously significant amounts of incomplete charge collection noise.

Considering other wide bandgap III-V materials, the energy resolutions achieved here with the AlInP photodiodes are poorer than has been achieved using a 200  $\mu\text{m}$  diameter, 10  $\mu\text{m}$  thick  $i$  layer GaAs  $p^+ - i - n^+$  photodiode (695 eV FWHM at 4.95 keV and 735 eV FWHM at 21.17 keV<sup>9</sup>) but are similar/better than with InGaP  $p^+ - i - n^+$  photodiodes with 5  $\mu\text{m}$  thick  $i$  layers (790 eV FWHM at 4.95 keV and 830 eV FWHM at 21.17 keV for a 200  $\mu\text{m}$  diameter detector; 1.12 keV FWHM at 4.95 keV and 1.15 keV FWHM at 21.17 keV for a 400  $\mu\text{m}$  diameter detector).<sup>14</sup> Since the electron-hole pair creation energies of these three materials differ (5.31 eV for AlInP,<sup>37</sup> 4.95 eV for InGaP,<sup>15</sup> and 4.179 eV for GaAs,<sup>39</sup> each at 30 °C), a comparison between the indicated total equivalent noise charges present in each spectrometer is informative. Considering the reported characteristics of 200  $\mu\text{m}$  diameter  $p^+ - i - n^+$  photodiodes made of each material (InGaP from Ref. 14 and GaAs from Ref. 9) and in each case operating at a temperature of 30 °C, the equivalent noise charge was 60  $e^-$  rms for AlInP (D1), 68  $e^-$  rms for InGaP, and 71  $e^-$  rms for GaAs at 4.95 keV, and 67  $e^-$  rms for AlInP, 71  $e^-$  rms for InGaP, and 75  $e^-$  rms for GaAs at 21.17 keV. Considering the characteristics of the 400  $\mu\text{m}$  diameter AlInP  $p^+ - i - n^+$  photodiodes (D2) and comparing them with InGaP devices of the same area,<sup>15</sup> the equivalent noise charges were 68  $e^-$  rms for AlInP and 96  $e^-$  rms for InGaP at 4.95 keV, and 71  $e^-$  rms for AlInP and 99  $e^-$  rms for InGaP at 21.17 keV. Thus, although the FWHM in energy terms (within the investigated energy range) achieved using D1 was poorer than that achieved with the (same area) GaAs detector<sup>9</sup> due to the larger electron-hole pair creation energy of AlInP, cf. GaAs, the equivalent noise charges of both D1 and D2 were lower (better) than that of the previously reported GaAs detector.<sup>9</sup> The equivalent noise charges of both D1 and D2 were also lower (better) than that achieved with the previously reported InGaP detectors.<sup>14</sup>

## V. LINEARITY RESPONSE OF THE DETECTED COUNT RATE

The detected count rate linearity was then investigated. X-ray fluorescence spectra were accumulated with the same experimental conditions as described above (Sec. IV) but using only the Zn fluorescence calibration foil and varying the Mo target x-ray tube current from 0.2 to 1.0 mA, in 0.2 mA steps. To increase the range of incident x-ray photon flux, in addition to varying the Mo target x-ray tube current of the x-ray apparatus, two different collimators were used; a 20 mm diameter collimator (the same collimator as that used for the energy calibration) and an 8 mm diameter collimator of the same design but which reduced the incident flux.

The detected count rates, measured in counts  $s^{-1}$ , were recorded as functions of x-ray tube current for both collimators and both detector systems. The number of detected counts was considered to be defined by the total number of counts within the fitted Gaussian of the Zn  $K\alpha$  (8.63 keV) photopeak (i.e., excluding other peaks and low-energy tailing resulting from the partial collection of the charge created outside of the  $i$  layer); this number of



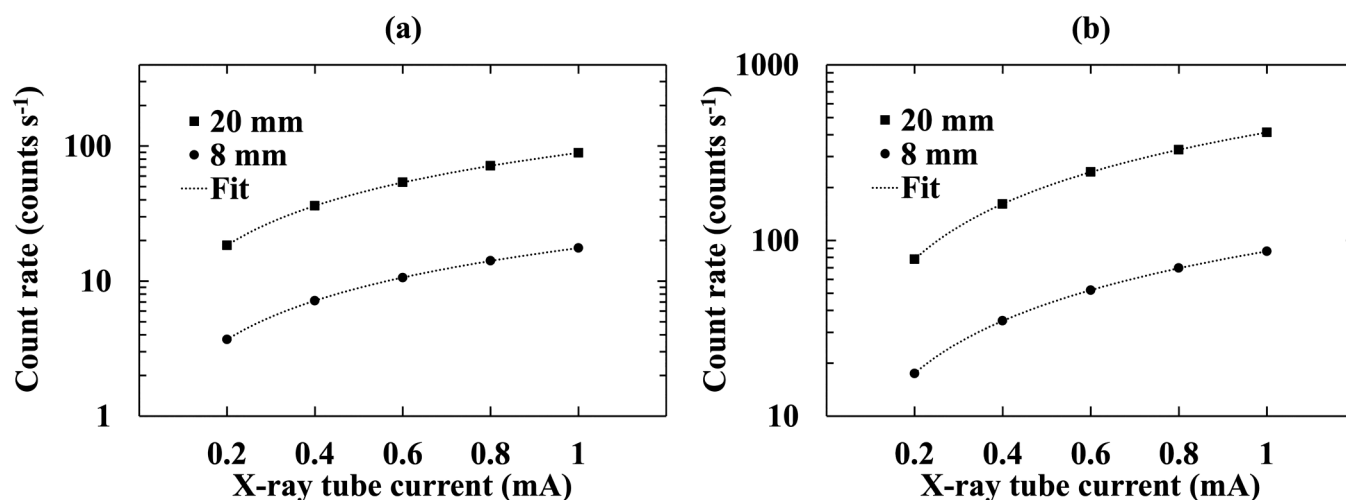


**FIG. 9.** Count rates (number of counts contained within the Gaussian fitted to the Zn  $K\alpha$  x-ray fluorescence peak divided by the spectrum accumulation time) as functions of x-ray tube current for (a) D1 and (b) D2. Collimators of two different diameters [20 mm (black squares) and an 8 mm (black circles)] were used to collimate the x-ray photons from the x-ray tube. The lines of the best fits (dotted lines), as determined using linear least squares fitting, are also shown.

counts was subsequently divided by the live time limit (9600 s for D1 and 2400 s for D2). The results are shown in Fig. 9. The relationships between the detected count rates and the incident x-ray photon fluxes in each case were determined by calculating the lines of best fit, using linear least squares fitting. These are also shown in Fig. 9. The suitability of fitting the count rates as a function of the x-ray tube current with a linear line was assessed; the error bars,  $S$ , of the fitting were calculated [using Eq. (2)] and then compared with the uncertainties of determining the count rates. The results can be seen in Table III.

The error bars,  $S$ , associated with the fitting of the linear line were smaller than the uncertainties of the experimentally determined count rates in each case. Thus, the results suggested that the reported x-ray spectrometers had linear detected count rates (at 8.63 keV) with incoming x-ray photon flux. The range of the incident photon flux that the linearity was investigated (and was found to be valid) was then estimated; the detected count rates and the quantum

detection efficiency of the detectors at 8.63 keV were taken into account. The quantum detection efficiencies at 8.63 keV of D1 and D2, when reverse biased at 150 V, were 0.306 and 0.309, respectively (see Fig. 2). D1 and D2 based x-ray spectrometers had linear responses at incident x-ray photon fluxes up to at least  $0.925 \times 10^6 \pm 0.003 \times 10^6$  photons  $s^{-1} cm^{-2}$  and  $1.062 \times 10^6 \pm 0.003 \times 10^6$  photons  $s^{-1} cm^{-2}$ , respectively. These maximum incident x-ray photon fluxes were achieved with an x-ray tube current of 1 mA and the 20 mm diameter collimator. The observed difference in the incident photon flux upon D1 and D2 was attributed to a slight difference in the placement of each detector within the experimental setup.

## VI. $^{241}\text{Am}$ AND $^{109}\text{Cd}$ RADIOISOTOPE X-RAY AND $\gamma$ -RAY SPECTRA

The spectroscopic performance of the detectors was then investigated at photon energies up to 88.03 keV. The detectors were connected, in turn, to a custom-made low-noise charge-sensitive preamplifier of the same design as that used in Secs. IV and V. The detector–preamplifier system was installed in a Temperature Applied Sciences Limited<sup>31</sup> Micro LT climatic cabinet for temperature control and operated at 30 °C. X-ray and  $\gamma$ -ray spectra were accumulated using an  $^{241}\text{Am}$  radioisotope x-ray and  $\gamma$ -ray source (299 MBq activity) and a  $^{109}\text{Cd}$  radioisotope x-ray and  $\gamma$ -ray source (371 MBq activity); each source was encapsulated in its own stainless steel capsule with a 250  $\mu\text{m}$  thick Be window. A live time limit of 24 h was set, along with a shaping time of 2  $\mu\text{s}$ . The detectors were each operated at 150 V applied reverse bias.

The  $^{241}\text{Am}$  x-ray and  $\gamma$ -ray spectra accumulated with D1 and D2 are shown in Fig. 10. The main characteristic emission lines of the  $^{241}\text{Am}$  radioisotope source were the x-ray  $\text{Np } L\alpha$  (at 13.95 and 13.76 keV),  $L\beta$  (ranging from 16.11 to 17.99 keV), and  $L\gamma$

**TABLE III.** Gradient, intercept point, and error bars,  $S$ , associated with the linear least squares fitting of the count rate as a function of x-ray tube current for D1 and D2, using both the 20 mm and the 8 mm diameter collimators. The uncertainty of the count rate in each case is also shown.

		$\pm$ Count rate (counts $s^{-1}$ )	Gradient (counts $s^{-1}$ $\text{mA}^{-1}$ )	Intercept point (counts $s^{-1}$ )	$S$ [Eq. (2)] (counts $s^{-1}$ )
D1	20 mm	>0.07	$88.34 \pm 0.08$	$0.73 \pm 0.06$	0.05
	8 mm	>0.03	$17.34 \pm 0.05$	$0.22 \pm 0.03$	0.03
D2	20 mm	>0.3	$417.5 \pm 0.4$	$-5.6 \pm 0.3$	0.2
	8 mm	>0.09	$86.6 \pm 0.1$	$0.20 \pm 0.09$	0.09

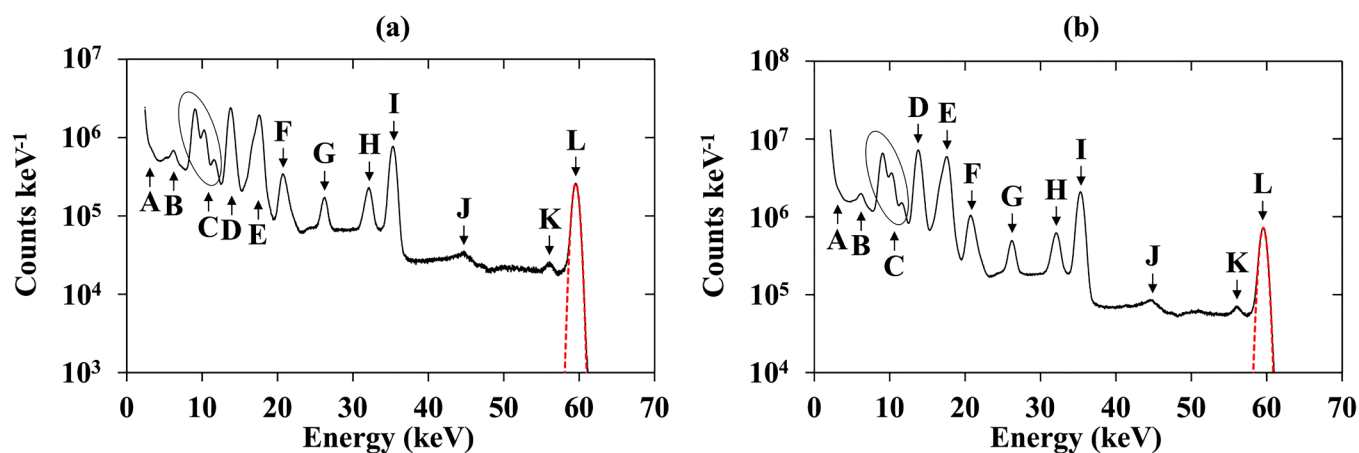


**FIG. 10.**  $^{241}\text{Am}$  x-ray and  $\gamma$ -ray spectra accumulated with (a) D1 and (b) D2 at 30 °C (150 V reverse bias, 2  $\mu\text{s}$  shaping time). The major peaks identified are (A) In L $\beta$  detector fluorescence, (B) Cr K $\alpha$  and Fe K $\alpha$  capsule fluorescence, (C) Ga K $\alpha$  and K $\beta$  and As K $\alpha$  and K $\beta$  detector fluorescence and escape from  $^{241}\text{Am}$  Np L $\beta$  and Np L $\gamma$  x-ray photons, (D)  $^{241}\text{Am}$  Np L $\alpha$ , (E)  $^{241}\text{Am}$  Np L $\beta$ , (F)  $^{241}\text{Am}$  Np L $\gamma$ , (G)  $^{241}\text{Am}$  26.3 keV  $\gamma$ -ray, (H)  $^{241}\text{Am}$  33.2 keV  $\gamma$ -ray, (I) In K $\alpha$  escape from  $^{241}\text{Am}$  59.54 keV  $\gamma$ -rays and pulse pile up from  $^{241}\text{Am}$  Np L $\beta$  x-ray photons, (J)  $^{241}\text{Am}$  43.4 keV  $\gamma$ -ray, (K) In L $\alpha$  and In L $\beta$  escape from  $^{241}\text{Am}$  59.54 keV  $\gamma$ -rays, and (L)  $^{241}\text{Am}$  59.54 keV  $\gamma$ -ray. The Gaussian fitted at the 59.54 keV  $\gamma$ -ray peak (red dashed line) is shown. The FWHM at 59.54 keV was  $1.02 \pm 0.05$  keV for D1 and  $1.07 \pm 0.05$  keV for D2.

(ranging from 20.78 to 21.49 keV) emission lines<sup>40</sup> and the  $\gamma$ -ray lines at 26.3, 33.2, 43.4, and 59.54 keV;<sup>41</sup> all of these emitted lines were detected by the spectrometer and are identified in Fig. 10. The  $\alpha$  particles emitted by the  $^{241}\text{Am}$  radioisotope source were completely absorbed by the Be window of the capsule. Gaussian fitting was applied to the 59.54 keV  $\gamma$ -ray peak; the centroid channel number of the fitted peak at 59.54 keV and the position of the zero energy noise peak were used to energy calibrate the MCA charge scale. The fitted Gaussian can also be seen in Fig. 10; the FWHM at 59.54 keV was  $1.02 \pm 0.05$  keV for D1 and  $1.07 \pm 0.05$  keV for D2.

X-ray fluorescence peaks from detector self-fluorescence, In L $\beta$ , Ga K $\alpha$  and K $\beta$ , and As K $\alpha$  and K $\beta$ , are visible in the spectra, as are fluorescence peaks from the stainless steel capsule, Fe K $\alpha$  and Cr K $\alpha$ , of the  $^{241}\text{Am}$  radioisotope source. Furthermore, Ga K $\alpha$  and K $\beta$  and As K $\alpha$  and K $\beta$  escape peaks from Np L $\beta$  and Np L $\gamma$  x-ray photons, and In K $\alpha$ , L $\alpha$ , and L $\beta$  escape peaks from 59.54 keV  $\gamma$ -ray photons are also present.

The  $^{109}\text{Cd}$  x-ray and  $\gamma$ -ray spectra accumulated with D1 and D2 are shown in Fig. 11. The main characteristic emission lines from the  $^{109}\text{Cd}$  radioisotope x-ray and  $\gamma$ -ray source were the Ag K $\alpha$  (22.16 and 21.99 keV), K $\beta$  (24.9 keV), and L $\alpha$  (2.98 keV) x rays and

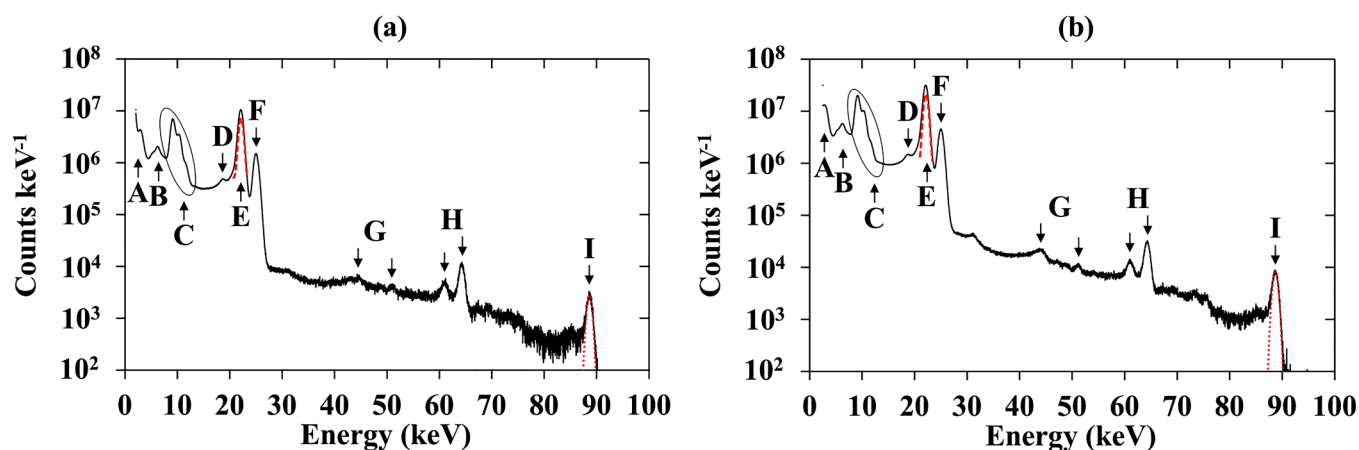


**FIG. 11.**  $^{109}\text{Cd}$  x-ray and  $\gamma$ -ray spectra accumulated with (a) D1 and (b) D2 at 30 °C (150 V reverse bias, 2  $\mu\text{s}$  shaping time). The major peaks are (A)  $^{109}\text{Cd}$  Ag L $\alpha$ , (B) Cr K $\alpha$  and Fe K $\alpha$  capsule fluorescence, (C) Ga K $\alpha$  and K $\beta$  and As K $\alpha$  and K $\beta$  detector fluorescence and escape from  $^{109}\text{Cd}$  Ag K $\alpha$  x-ray photons, (D) In L $\beta$  escape from  $^{109}\text{Cd}$  Ag K $\alpha$  x-ray photons, (E)  $^{109}\text{Cd}$  Ag K $\alpha_1$  and K $\alpha_2$ , (F)  $^{109}\text{Cd}$  Ag K $\beta$ , (G) pulse pile up from  $^{109}\text{Cd}$  Ag K $\alpha$  and K $\beta$  x-ray photons, (H) In K $\alpha$  and K $\beta$  escape from  $^{109}\text{Cd}$  88.03 keV  $\gamma$ -rays, and (I)  $^{109}\text{Cd}$  88.03 keV  $\gamma$ -ray. The Gaussians fitted at the Ag K $\alpha_1$  peak (red dashed line) and at the 88.03 keV  $\gamma$ -ray peak (red dotted line) are shown.

**TABLE IV.** FWHM and the calculated total noise excluding the Fano noise (quadratic sum of electronic noise and, if present, incomplete charge collection noise).

	FWHM (keV) $\pm$ 0.05 keV at			FWHM (keV) excl. Fano noise at		
	22.16 keV	59.54 keV	88.03 keV	22.16 keV	59.54 keV	88.03 keV
D1	0.94	1.02	1.07	$0.89 \pm 0.05$	$0.90 \pm 0.05$	$0.90 \pm 0.06$
D2	0.99	1.07	1.13	$0.95 \pm 0.05$	$0.96 \pm 0.06$	$0.97 \pm 0.06$

the 88.03 keV  $\gamma$ -rays;<sup>42</sup> all were detected and are identified in the spectra presented in Fig. 11. The Ag  $K\alpha$  peak was the combination of the Ag  $K\alpha_1$  and  $K\alpha_2$  lines; Gaussians were fitted to the combined Ag  $K\alpha_1$  and  $K\alpha_2$  peaks, taking into account the relative emission ratio and the relative quantum detection efficiency of the detectors at 22.16 and 21.99 keV. The centroid channel number of the fitted peak at 22.16 keV and the position of the zero energy noise peak were used to energy calibrate the MCA charge scale. The fitted Gaussian at 22.16 keV is also shown in Fig. 11; the FWHM at 22.16 keV was  $0.94 \pm 0.05$  keV for D1 and  $0.99 \pm 0.05$  keV for D2. The 88.03 keV  $\gamma$ -ray peak was also fitted with a Gaussian; FWHMs at 88.03 keV of  $1.07 \pm 0.05$  keV and  $1.13 \pm 0.05$  keV were measured for D1 and D2, respectively.

As per the <sup>241</sup>Am x-ray and  $\gamma$ -ray spectra, the detector self-fluorescence x rays and the fluorescence x rays from the stainless steel capsule of the <sup>109</sup>Cd radioisotope x-ray and  $\gamma$ -ray source were detected; Ga  $K\alpha$  and  $K\beta$ , As  $K\alpha$  and  $K\beta$ , Fe  $K\alpha$ , and Cr  $K\alpha$  fluorescence peaks can be seen in the spectra of Fig. 11. Additionally, Ga  $K\alpha$  and  $K\beta$ , As  $K\alpha$  and  $K\beta$ , and In  $L\beta$  escape peaks associated with the Ag  $K\alpha$  peak were detected. Escape peaks, In  $K\alpha$  and  $K\beta$  associated with the 88.03 keV  $\gamma$ -ray photons, were also observed. Finally, two additional peaks (at  $\approx 44$  and  $\approx 50$  keV) were attributed to Ag  $K\alpha$  and  $K\beta$  x-ray pulse pileup.<sup>43</sup>

It has been previously observed and reported that the incomplete charge collection, as a ballistic deficit effect, gives rise to a tail in the left-hand side of the photopeaks.<sup>28,44</sup> Even though no such low-energy shoulder was observed in the spectra presented in Figs. 10 and 11, the presence of incomplete charge collection noise cannot be entirely excluded; when its contribution is smaller than the other noise sources, it can be described as a Gaussian source and it may only result in the broadening of the photopeak, as it was the case for the 6  $\mu$ m thick i layer AlInP detector reported in Ref. 27. Additionally, although analysis of the spectra of x-ray fluorescence photons from the high-purity x-ray calibration foils accumulated with D1 and D2 suggested the absence of detectable incomplete charge collection noise up to 21.17 keV ( $<31$  e<sup>-</sup> rms for D1 and  $<25$  e<sup>-</sup> rms for D2), incomplete charge collection noise may become significant at higher energies. The energy resolution, FWHM, as a function of photon energy as determined from the <sup>241</sup>Am and <sup>109</sup>Cd x-ray and  $\gamma$ -ray spectra allowed the investigation of the presence of the significant incomplete charge collection at both detectors operating at 150 V reverse bias, for photon energies up to 88.03 keV.

In addition to the incomplete charge collection noise, the Fano noise is photon energy,  $E$ , dependent, whereas the electronic noise is independent of the incident photon energy [see Eq. (1)]. Thus, the dependency (or not) of the total noise excluding the Fano noise upon the photon energy suggests the presence (or not) of the

incomplete charge collection noise. The Fano noise was subtracted in quadrature from the total noise at each investigated energy (22.16, 59.54, and 88.03 keV), and the remainder was attributed to the combined contribution of the electronic noise and (if any) incomplete charge collection noise. However, it should be noted that a measurement of the Fano factor in Al<sub>0.52</sub>In<sub>0.48</sub>P has not yet been reported, and as such, the value for In<sub>0.5</sub>Ga<sub>0.5</sub>P (=0.13) was used here. A summary of the total measured noise and the total noise, excluding the Fano noise for both detectors, can be seen in Table IV.

The mean of the total noise excluding the Fano noise across the investigated energy range was  $895 \pm 5$  eV (rms error) for D1 and  $960 \pm 10$  eV (rms error) for D2. Considering the uncertainties related to determining the FWHM at each energy ( $\pm 50$  eV) and the rms error of the mean of the total noise excluding the Fano noise, the latter was photon energy invariant. As such, the absence of significant incomplete charge collection noise was suggested up to 88.03 keV photon energy, when the detectors were reverse biased at 150 V; the electronic noise could thus be inferred. The electronic noise was  $890 \pm 30$  eV and  $960 \pm 30$  eV for D1 and D2 based spectrometers, respectively. These values were greater compared to the electronic noise extracted from the fitting of Eq. (1) to the data presented in Fig. 8 (755 eV for D1; 837 eV for D2). However, while the preamplifier of the spectrometer used to detect photons from the <sup>109</sup>Cd and <sup>241</sup>Am radioisotope x-ray and  $\gamma$ -ray sources was of the same design, it was not the same specific preamplifier instance as was used to detect the x-ray fluorescence photons from high-purity metal calibration foils (results reported in Secs. IV and V). Variations in performance between preamplifiers of this type—even when they are of identical design—is a known phenomenon; it arises mainly due to subtle variations in the input JFET used in each preamplifier on a device to device basis, even for JFETs of the same model and manufacture. This explained the difference between the extracted electronic noises of each spectrometer when the same detector was used in different parts of the investigation.

## VII. CONCLUSIONS

The spectroscopic response of the thickest (10  $\mu$ m i layer) AlInP x-ray and  $\gamma$ -ray detectors so far reported has been studied across the photon energy range from 4.95 to 88.03 keV, under the illumination of x-ray fluorescence photons from high-purity metal calibration foils and x-ray and  $\gamma$ -ray photons from radioisotope sources. This is also the widest energy range so far reported for AlInP x-ray and  $\gamma$ -ray detectors. The detectors (200  $\mu$ m diameter, D1; 400  $\mu$ m diameter, D2), along with the preamplifier, were operated uncooled, at 30 °C, and were found to possess promising electronic and spectroscopic characteristics and performance.

The white parallel and white series noise contributions of the photodiodes themselves (i.e., excluding that of the packaging) at their normal operating conditions (30 °C, 150 V applied reverse bias, 2  $\mu$ s shaping time) were found to be small compared with other noise contributors. One of the detectors, D1, contributed  $6 \pm 5$  e<sup>-</sup> rms of white parallel noise and  $2.3 \pm 0.2$  e<sup>-</sup> rms of white series noise to the energy resolution of the spectrometer. Similarly, the electronic noise contribution D2 to the energy resolution of the spectrometer was  $2.3 \pm 0.2$  e<sup>-</sup> rms for white parallel noise and  $9.0 \pm 0.2$  e<sup>-</sup> rms for white series noise.

Both detectors were coupled, in turn, to a custom charge-sensitive preamplifier and electronics chain configured to be suitable for illumination of the detector with x-ray fluorescence photons (energies ranging from 4.95 to 21.17 keV) from high-purity metal calibration foils. Linear relationships between the incoming x-ray photon energy (up to 21.17 keV, which was the highest energy investigated in this way) and the charge output of the spectroscopic systems employing the detectors, within  $\pm 40$  eV for D1 and  $\pm 14$  eV for D2 over the energy,  $E$ , range  $4.95 \text{ keV} \leq E \leq 21.17 \text{ keV}$ , were found. The energy resolution (FWHM) degraded as a function of increasing x-ray photon energy for both spectroscopic systems: from  $750 \pm 40$  eV at 4.95 keV to  $840 \pm 40$  eV at 21.17 keV for the spectrometer employing D1 and from  $850 \pm 30$  eV at 4.95 keV to  $890 \pm 30$  eV at 21.17 keV for the spectrometer employing D2. The investigation of the presence of incomplete charge collection noise within the explored photon energy range suggested that the observed increase of the FWHM with increasing energy was consistent with the increase in the Fano noise alone. Unlike the thinner (2  $\mu$ m i layer) AlInP devices,<sup>27,28</sup> but similar to previously reported 6  $\mu$ m i layer thick AlInP devices,<sup>28</sup> the currently reported detectors did not show signs of any detectable incomplete charge collection when reverse biased at 150 V; the limits of any present but undetectable incomplete charge collection noise were calculated to be  $<31$  e<sup>-</sup> rms (for D1) and  $<25$  e<sup>-</sup> rms (for D2) at 21.17 keV, which was the greatest energy and thus that at which the maximum incomplete charge collection noise would have been present. Linear increases of the count rate at 8.63 keV (Zn K $\alpha$ ) were recorded for x-ray photon fluxes up to the maxima investigated, i.e.,  $0.925 \times 10^6 \pm 0.003 \times 10^6$  photons s<sup>-1</sup> cm<sup>-2</sup> (for D1) and  $1.062 \times 10^6 \pm 0.003 \times 10^6$  photons s<sup>-1</sup> cm<sup>-2</sup> (for D2).

Each detector was then coupled, in turn, to another preamplifier and electronics chain, which was configured in such a way as to be suitable for illumination of the detectors with photons from radioisotope x-ray and  $\gamma$ -ray sources; <sup>109</sup>Cd and <sup>241</sup>Am radioisotope x-ray and  $\gamma$ -ray sources were used. In addition to photopeaks corresponding to the characteristic emission lines of the sources, detector self-fluorescence and source capsule fluorescence peaks, as well as escape peaks, were present in the accumulated spectra. The energy resolution increased from  $0.94 \pm 0.05$  keV at 22.16 keV to  $1.02 \pm 0.05$  keV at 59.54 keV and then to  $1.07 \pm 0.05$  keV at 88.03 keV for D1. Similarly, the energy resolution degraded with increasing photon energy for D2, i.e., from  $0.99 \pm 0.05$  keV at 22.16 keV to  $1.07 \pm 0.05$  keV at 59.54 keV and then to  $1.13 \pm 0.05$  keV at 88.03 keV. Analysis of these results again suggested the presence of an insignificant incomplete charge collection noise up to 88.03 keV, when the detectors were reverse biased at 150 V.

In summary, the reported AlInP detectors were operated uncooled (at 30 °C) and investigated in detail at photon energies up to 88.03 keV. The detectors were found to be suitable for photon counting x-ray and  $\gamma$ -ray spectroscopy with linear responses as functions of incoming photon energy. AlInP detectors have thus been shown to be viable candidate detectors for future x-ray and  $\gamma$ -ray spectrometers for real world deployment. Improved energy resolutions and increased quantum detection efficiencies were recorded for D1 and D2 compared to earlier and thinner (2 and 6  $\mu$ m thick i layers) AlInP detectors. Such results are important, particularly for x-ray fluorescence spectroscopy for quantitative elemental analysis, for example, in space science applications<sup>45</sup> as well as terrestrial geology<sup>46</sup> and ocean exploration.<sup>9</sup> Thick (i layer thickness  $>10 \mu$ m) Al<sub>0.52</sub>In<sub>0.48</sub>P detectors will be developed. The experiments anticipated to be conducted with such devices include measurements of the carrier mobilities, lifetimes, and their products, in the materials grown; these can then be compared with previously reported values.<sup>47</sup> Such measurements, coupled with modeling of charge cloud physics and other detector processes,<sup>48,49</sup> and measurements of the detectors' charge output linearity and energy resolution as functions of photon energy using synchrotron x-ray sources (which can be adjusted in  $\sim 1$  eV energy steps)<sup>49</sup> would help establish the fundamental performance limits of Al<sub>0.52</sub>In<sub>0.48</sub>P x-ray and  $\gamma$ -ray photodiodes. Determination of the maximum useful detector thickness (limited by carrier transport) is a particularly important part of establishing the viability of Al<sub>0.52</sub>In<sub>0.48</sub>P as a material for high energy  $\gamma$ -ray detection.

## ACKNOWLEDGMENTS

This work was supported by the Science and Technology Facilities Council, United Kingdom, through Grant Nos. ST/R001804/1 and ST/T000910/1, and the Engineering and Physical Sciences Research Council, United Kingdom, through Grant No. EP/P021271/1 (University of Sussex: A.M. Barnett, Principal Investigator). A.M.B. acknowledges funding from the Leverhulme Trust in the form of a 2016 Philip Leverhulme Prize. The authors are grateful to R. J. Airey and S. Kumar at the EPSRC National Epitaxy Facility for device fabrication and to M. D. C. Whitaker at the University of Sussex for useful suggestions to improve the manuscript.

## DATA AVAILABILITY

The data that support the findings of this study are available within the article.

## REFERENCES

- <sup>1</sup>N. Wermes, L. Andricek, P. Fischer, M. Harter, S. Herrmann, M. Karagounis, R. Kohrs, H. Kruger, G. Lutz, P. Lechner, I. Peric, M. Porro, R. Richter, H. Soltau, L. Struder, M. Trimpl, J. Ulrici, and J. Treis, *IEEE Trans. Nucl. Sci.* **51**, 1121 (2004).
- <sup>2</sup>R. Redus, A. Huber, J. Pantazis, and T. Pantazis, in *IEEE Nuclear Science Symposium and Medical Imaging Conference (NSS/MIC), Valencia, Spain, 23–29 October* (IEEE, 2011), p. 580.
- <sup>3</sup>H. Oyanagi, M. Martini, and M. Saito, *Nucl. Instrum. Methods Phys. Res. Sect. A* **403**, 58 (1998).
- <sup>4</sup>G. Bertuccio, S. Caccia, D. Puglisi, and D. Macera, *Nucl. Instrum. Methods Phys. Res. Sect. A* **652**, 193 (2011).

- <sup>5</sup>G. S. Zhao, G. Lioliou, and A. M. Barnett, *Nucl. Instrum. Methods Phys. Res. Sect. A* **859**, 76 (2017).
- <sup>6</sup>A. Owens, M. Bavdaz, A. Peacock, A. Poelaert, H. Andersson, S. Nenonen, H. Sipilä, L. Tröger, and G. Bertuccio, *J. Appl. Phys.* **90**, 5376 (2001).
- <sup>7</sup>C. Erd, A. Owens, G. Brammertz, M. Bavdaz, A. Peacock, V. Lämsä, S. Nenonen, H. Andersson, and N. Haack, *Nucl. Instrum. Methods Phys. Res. Sect. A* **487**, 78 (2002).
- <sup>8</sup>G. Lioliou, M. D. C. Whitaker, and A. M. Barnett, *J. Appl. Phys.* **122**, 244506 (2017).
- <sup>9</sup>G. Lioliou and A. M. Barnett, *X-Ray Spectrom.* **47**, 201 (2018).
- <sup>10</sup>G. Lioliou and A. M. Barnett, *Nucl. Instrum. Methods Phys. Res. Sect. A* **985**, 164672 (2021).
- <sup>11</sup>A. M. Barnett, J. E. Lees, D. J. Bassford, J. S. Ng, C. H. Tan, N. Babazadeh, and R. B. Gomes, *Nucl. Instrum. Methods Phys. Res. Sect. A* **654**, 336 (2011).
- <sup>12</sup>M. D. C. Whitaker, G. Lioliou, and A. M. Barnett, *Nucl. Instrum. Methods Phys. Res. Sect. A* **899**, 106 (2018).
- <sup>13</sup>M. D. C. Whitaker, G. Lioliou, A. B. Krysa, and A. M. Barnett, *Semicond. Sci. Technol.* **35**, 095026 (2020).
- <sup>14</sup>G. Lioliou, A. B. Krysa, and A. M. Barnett, *J. Appl. Phys.* **124**, 195704 (2018).
- <sup>15</sup>S. Butera, G. Lioliou, A. B. Krysa, and A. M. Barnett, *Nucl. Instrum. Methods Phys. Res. Sect. A* **908**, 277 (2018).
- <sup>16</sup>A. Zappettini, D. Macera, G. Benassi, N. Zambelli, D. Calestani, M. Ahangarianabhari, Y. Shi, G. Rotondo, B. Garavelli, P. Pozzi, and G. Bertuccio, in *IEEE Nuclear Science Symposium and Medical Imaging Conference (NSS/MIC)*, Seattle, WA, 8–15 November (IEEE, 2014).
- <sup>17</sup>L. Abbene, G. Gerardi, G. Raso, F. Principato, N. Zambelli, G. Benassi, M. Bettelli, and A. Zappettini, *J. Synchrotron Radiat.* **24**, 429 (2017).
- <sup>18</sup>J. H. Hubbell and S. M. Seltzer, *Tables of X-Ray Mass Attenuation Coefficients and Mass Energy-Absorption Coefficients (Version 1.4)* (National Institute of Standards and Technology, Gaithersburg, MD, 2004).
- <sup>19</sup>J. S. Cheong, J. S. L. Ong, J. S. Ng, A. B. Krysa, and J. P. R. David, *IEEE J. Sel. Top. Quantum Electron.* **20**, 142 (2014).
- <sup>20</sup>W. Bludau, A. Onton, and W. Heinke, *J. Appl. Phys.* **45**, 1846 (1974).
- <sup>21</sup>S. M. Sze and K. K. Ng, *Physics of Semiconductor Devices*, 3rd ed. (John Wiley & Sons, 2007).
- <sup>22</sup>J. S. L. Ong, J. S. Ng, A. B. Krysa, and J. P. R. David, *IEEE Electron Device Lett.* **32**, 1528 (2011).
- <sup>23</sup>S. Butera, G. Lioliou, A. B. Krysa, and A. M. Barnett, *J. Appl. Phys.* **120**, 024502 (2016).
- <sup>24</sup>S. Butera, T. Gohil, G. Lioliou, A. B. Krysa, and A. M. Barnett, *J. Appl. Phys.* **120**, 174503 (2016).
- <sup>25</sup>S. Zhao, S. Butera, G. Lioliou, A. B. Krysa, and A. M. Barnett, *J. Phys. D: Appl. Phys.* **52**, 225101 (2019).
- <sup>26</sup>S. Zhao, S. Butera, G. Lioliou, A. B. Krysa, and A. M. Barnett, *Sci. Rep.* **9**, 12155 (2019).
- <sup>27</sup>G. Lioliou, S. Butera, A. B. Krysa, and A. M. Barnett, *Nucl. Instrum. Methods Phys. Res. Sect. A* **943**, 162467 (2019).
- <sup>28</sup>S. Zhao, G. Lioliou, S. Butera, A. B. Krysa, and A. M. Barnett, *Nucl. Instrum. Methods Phys. Res. Sect. A* **960**, 163606 (2020).
- <sup>29</sup>A. M. Barnett, *Nucl. Instrum. Methods Phys. Res. Sect. A* **756**, 39 (2014).
- <sup>30</sup>G. Lioliou and A. M. Barnett, *Nucl. Instrum. Methods Phys. Res. Sect. A* **801**, 63 (2015).
- <sup>31</sup>Temperature Applied Sciences Ltd, Goring Business Park, Goring-by-Sea, West Sussex, BN12 4HF, England, United Kingdom.
- <sup>32</sup>A. M. Barnett, D. J. Bassford, J. E. Lees, J. S. Ng, C. H. Tan, and J. P. R. David, *Nucl. Instrum. Methods Phys. Res. Sect. A* **621**, 453 (2010).
- <sup>33</sup>G. Bertuccio, P. Rehak, and D. Xi, *Nucl. Instrum. Methods Phys. Res. Sect. A* **326**, 71 (1993).
- <sup>34</sup>A. Thompson, D. Attwood, E. Gullikson, M. Howells, K. J. Kim, J. Kirz, J. Kortright, I. Lindau, Y. Liu, P. Pianetta, A. Robinson, J. Scofield, J. Underwood, G. Williams, and H. Winick, *X-ray Data Booklet (Centre for X-Ray Optics and Advanced Light Source)* (Lawrence Berkeley National Laboratory, Berkeley, CA, 2009).
- <sup>35</sup>M. Sánchez del Río, A. Brunetti, B. Golosio, A. Somogyi, and A. Simionovici, *XRAYLIB Tables (X-Ray Fluorescence Cross Section)* (European Synchrotron Radiation Facility and University of Sassari, 2003).
- <sup>36</sup>G. Bertuccio, A. Pullia, and G. De Geronimo, *Nucl. Instrum. Methods Phys. Res. Sect. A* **380**, 301 (1996).
- <sup>37</sup>S. Butera, G. Lioliou, A. B. Krysa, and A. M. Barnett, *Nucl. Instrum. Methods Phys. Res. Sect. A* **879**, 64 (2017).
- <sup>38</sup>N. R. Draper and H. Smith, *Applied Regression Analysis*, 3rd ed. (John Wiley & Sons, 1998).
- <sup>39</sup>G. Bertuccio and D. Maiocchi, *J. Appl. Phys.* **92**, 1248 (2002).
- <sup>40</sup>H. Verma, *Appl. Radiat. Isot.* **122**, 41 (2017).
- <sup>41</sup>M. M. Be, V. Chiste, C. Dulieu, X. Mougeot, E. Browne, V. Chechev, N. Kuzmenko, F. Kondev, A. Luca, M. Galan, A. L. Nichols, A. Arinc, and X. Huang, *Monographie BIPM-5*, 5 (2010).
- <sup>42</sup>H. Xiaolong, Y. Shenggui, and D. Chunsheng, *Nucl. Instrum. Methods Phys. Res. Sect. A* **621**, 443 (2010).
- <sup>43</sup>G. F. Knoll, *Radiation Detection and Measurements*, 4th ed. (John Wiley & Sons, 2010).
- <sup>44</sup>M. Sarmartini, M. Gandola, F. Mele, B. Garavelli, D. Macera, P. Pozzi, and G. Bertuccio, *IEEE Trans. Nucl. Sci.* **68**, 70 (2021).
- <sup>45</sup>T. Arai, T. Okada, Y. Yamamoto, K. Ogawa, K. Shirai, and M. Kato, *Earth Planets Space* **60**, 21 (2008).
- <sup>46</sup>K. E. Young, C. A. Evans, K. V. Hodges, J. E. Bleacher, and T. G. Graff, *Appl. Geochem.* **72**, 77 (2016).
- <sup>47</sup>J. S. Cheong, J. S. L. Ong, J. S. Ng, A. B. Krysa, F. Bastiman, and J. P. R. David, *Proc. SPIE* **8899**, 88990G (2013).
- <sup>48</sup>J. E. Lees, *Nucl. Instrum. Methods Phys. Res. Sect. A* **613**, 98 (2010).
- <sup>49</sup>G. W. Fraser, A. F. Abbey, A. Holland, K. McCarthy, A. Owens, and A. Wells, *Nucl. Instrum. Methods Phys. Res. Sect. A* **350**, 368 (1994).